Geochemistry Geophysics Geosystems G3

Article
Volume 11
8 June 2010
Q0AB05, doi:10.1029/2010GC003036
ISSN: 1525-2027

Published by AGU and the Geochemical Society

Melt-induced seismic anisotropy and magma assisted rifting in Ethiopia: Evidence from surface waves

I. D. Bastow
Department of Earth Sciences, University of Bristol, Bristol BS8 1RJ, UK (ian.bastow@bristol.ac.uk)

S. Pilidou
Cyprus Geological Survey, 1415 Lefkosia, Cyprus

J.-M. Kendall
Department of Earth Sciences, University of Bristol, Bristol BS8 1RJ, UK

G. W. Stuart
School of Earth and Environment, University of Leeds, Leeds LS6 9JT, UK

[1] The East African rift in Ethiopia is unique worldwide because it captures the final stages of transition from continental rifting to seafloor spreading. A recent study there has shown that magma intrusion plays an important role during the final stages of continental breakup, but the mechanism by which it is incorporated into the extending plate remains ambiguous: wide-angle seismic data and complementary geophysical tools such as gravity analysis are not strongly sensitive to the geometry of subsurface melt intrusions. Studies of shear wave splitting in near-vertical *SKS* phases beneath the transitional Main Ethiopian Rift (MER) provide strong and consistent evidence for a rift-parallel fast anisotropic direction. However, it is difficult to discriminate between oriented melt pocket (OMP) and lattice preferred orientation (LPO) causes of anisotropy based on *SKS* study alone. The speeds of horizontally propagating Love (S_H) and Rayleigh (S_V) waves vary in similar fashions with azimuth for LPO- and OMP-induced anisotropy, but their relative change is distinctive for each mechanism. This diagnostic is exploited by studying the propagation of surface waves from a suite of azimuths across the MER. Anisotropy is roughly perpendicular to the absolute plate motion direction, thus ruling out anisotropy due to the slowly moving African Plate. Instead, three mechanisms for anisotropy act beneath the MER: periodic thin layering of seismically fast and slow material in the uppermost ~10 km, OMP between ~20–75 km depth, and olivine LPO in the upper mantle beneath. The results are explained best by a model in which low aspect ratio melt inclusions (dykes and veins) are being intruded into an extending plate during late stage breakup. The observations from Ethiopia join a growing body of evidence from rifts and passive margins worldwide that shows magma intrusion plays an important role in accommodating extension without marked crustal thinning.

Components: 11,100 words, 9 figures, 3 tables.

Keywords: Ethiopia; rifting; lithosphere; seismic anisotropy; surface wave inversion; melt intrusion.

Index Terms: 1734 History of Geophysics: Seismology (0905); 8109 Tectonophysics: Continental tectonics: extensional (0905); 7255 Seismology: Surface waves and free oscillations.

Received 13 January 2010; **Revised** 5 April 2010; **Accepted** 8 April 2010; **Published** 8 June 2010.

Bastow, I. D., S. Pilidou, J.-M. Kendall, and G. W. Stuart (2010), Melt-induced seismic anisotropy and magma assisted rifting in Ethiopia: Evidence from surface waves, *Geochem. Geophys. Geosyst.*, *11*, Q0AB05, doi:10.1029/2010GC003036.

Theme: Magma-Rich Extensional Regimes
Guest Editors: R. Meyer, J. van Wijk, A. Breivik, and C. Tegner

1. Introduction

1.1. Overview

[2] Passive margins worldwide are often termed "magmatic margins" because they are characterized by thick sequences of extruded, intruded, and underplated igneous rocks emplaced prior to, or during rifting [e.g., *Coffin and Eldholm*, 1994; *Menzies et al.*, 2002]. Recent advances in wide-angle studies [e.g., *Maresh and White*, 2005; *White et al.*, 2008] mean that the structures lying beneath the seaward dipping reflectors that traditionally preclude view of the continent-ocean transition beneath passive margins, can now be imaged more clearly. In addition to large volumes of extruded rocks, even larger volumes can be intruded into the continental crust at the time of breakup [e.g., *White et al.*, 2008; *White and Smith*, 2009]. Less evolved continental rifts, such as the Baikal rift that are not characterized by broad-scale mantle thermal anomalies also show evidence that the lower crust is characterized by high reflectivity and high seismic velocities resulting from magma intrusion [e.g., *Thybo and Nielsen*, 2009; *Nielsen and Thybo*, 2009]. Collectively these studies reveal a previously poorly understood role for magma during continental breakup with significant implications for estimation of stretching factors and modeling of sedimentary basins around failed rifts [e.g., *Thybo and Nielsen*, 2009; *Nielsen and Thybo*, 2009].

[3] The Main Ethiopian rift (MER) captures the final stages of the transition between continental rifting and seafloor spreading above a mantle hot spot (Figure 1) [e.g., *Ebinger*, 2005]. The recent Ethiopia Afar Geoscientific Lithospheric Experiment (EAGLE) probed this region using passive and controlled source seismic techniques complemented by gravity and magnetotelluric studies [see, e.g., *Bastow et al.*, 2010, and references therein]. Results from EAGLE imply the presence of high-velocity [*Mackenzie et al.*, 2005; *Maguire et al.*, 2006], high-density [*Tiberi et al.*, 2005; *Cornwell et al.*, 2006; *Mickus et al.*, 2007] crustal intrusions sourced from a hot, partially molten upper mantle [e.g., *Bastow et al.*, 2005, 2008] with possible connection to the deeper African superplume [e.g., *Ritsema and van Heijst*, 2000; *Grand*, 2002; *Benoit et al.*, 2006; *Montelli et al.*, 2006; *Simmons et al.*, 2007; *Li et al.*, 2008]. Ongoing magmatic processes in the region are indicated strongly by the presence of crustal melt zones inferred from magnetotelluric study [*Whaler and Hautot*, 2006], and the spatial coincidence of seismicity in and around the MER with these zones of inferred partial melt [*Keir et al.*, 2009a]. However, most of the geophysical techniques used to date in Ethiopia are sensitive primarily to bulk crustal properties (crustal thickness, V_P, V_S etc) that do not unambiguously constrain the geometry of melt beneath the rift.

[4] An *SKS* shear wave splitting study by *Kendall et al.* [2005] (Figure 2) shows that the MER is one of the most anisotropic regions worldwide, with splitting delay times (δt) as high as ~3 s. Intriguingly, the change in orientation of fast *SKS* waves from the plateau regions to the MER mirrors a shift from N130°E directed extension to N110°E directed extension at ~2 Ma, when crustal strain localized toward the volcanically active Wonjii Fault Belt (WFB) [e.g., *Wolfenden et al.*, 2004]. Alternatively, analog modeling of deformation in Ethiopia [*Corti*, 2008] shows that the same evolution in structural trends since the Mid-Miocene can be obtained by uniformly directed N110°E extension of the lithosphere with early border fault structural trends controlled by preexisting lithospheric structural inheritances buried beneath Cenozoic flood basalts, with no need to invoke melt hypotheses. Either way, the *SKS* results provide compelling evidence to suggest that anisotropy in the MER is sensitive to evolving extensional processes. While *SKS* studies provide excellent lateral resolution of seismic anisotropy, depth resolution is relatively poor [e.g., *Bastow et al.*, 2007]. Discrimination between olivine lattice preferred orientation (LPO), fossil lithospheric anisotropy, and anisotropy due to oriented melt pockets (OMP) also remains enigmatic and it is here that this study seeks improvement.

[5] Surface waves are an ideal tool for studying the depth-dependent Earth structure along given azimuths on the Earth's surface. Rayleigh waves

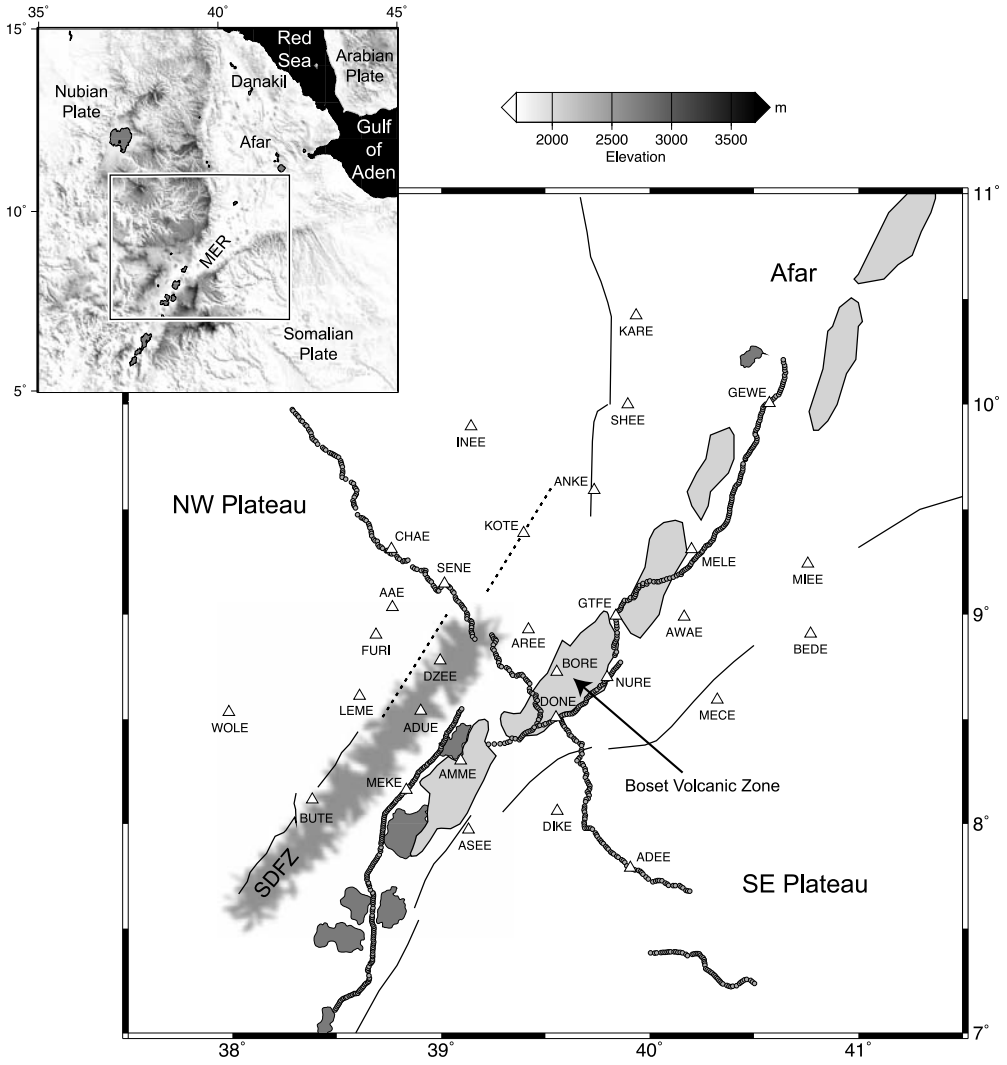

Figure 1. Location map of Ethiopia. Major Mid-Miocene border faults and Quaternary magmatic zones along the Wonjii Fault Belt (WFB) are shaded grey and delineated by the heavy black lines; dashed lines are faulted monoclines. Lakes are shown in dark grey. SDFZ, Silti Debre Zeit Fault Zone [e.g., *Rooney*, 2010]. Triangles are locations of broadband seismic stations. Grey dots are the locations of the EAGLE wide-angle profiles [*Maguire et al.*, 2006]. Inset shows the regional tectonic setting and topography.

sample S_V and Love waves sample S_H, and are sensitive to the mechanisms of anisotropy. Regional surface wave study to date in Ethiopia has been limited to isotropic Rayleigh wave analysis that provides support for upper mantle low velocities beneath Afar [*Knox et al.*, 1998; *Debayle et al.*, 2001; *Pasyanos and Nyblade*, 2007; *Priestley et al.*, 2008]. When analyzed jointly with receiver functions, surface wave study shows that V_S is 3.6–3.8 kms^{-1} in the lowermost crust and 4.3 kms^{-1} in the uppermost mantle, both 0.3 kms^{-1} lower than in the eastern and western branches of the East African Rift System to the south [*Dugda et al.*, 2007; *Keranen et al.*, 2009]. By analyzing the interstation phase velocities of Rayleigh and Love waves across the MER we provide strong evidence for melt intrusion related OMP-type anisotropy in the MER lithosphere. These observations corroborate the inferences of other geophysical studies and lend support to geochemical analyses of Quaternary eruptives that point toward the existence of a dyked/veined plumbing system beneath the MER [e.g., *Rooney et al.*, 2005, 2007].

1.2. Tectonic Setting

[6] Volcanism during the Cenozoic first affected East Africa in SW Ethiopia and northernmost Kenya at ~40–45 Ma [e.g., *Ebinger et al.*, 1993; *George et al.*, 1998; *Furman et al.*, 2006] before

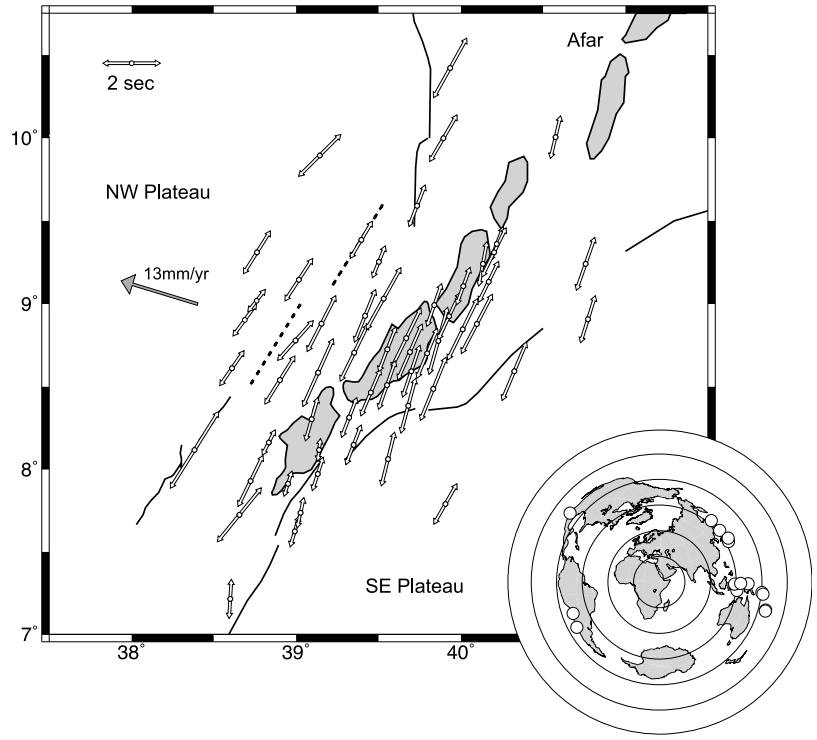

Figure 2. *SKS* splitting observations in the Ethiopian Rift. The orientation of arrows shows the alignment of fast shear waves; the length of the arrow is proportional to the magnitude of the splitting. Major Mid-Miocene border faults and Quaternary magmatic zones along the Wonjii Fault Belt (WFB) are shaded grey and delineated by the heavy black lines; dashed lines are faulted monoclines. Large grey arrow shows the absolute plate motion. Inset shows locations of earthquakes used for shear wave splitting analysis. Concentric circles mark 30° increments in distance from the EAGLE network. Adapted by permission from Macmillan Publishers Ltd.: *Kendall et al.* [2005], copyright 2005, and modified after *Kendall et al.* [2006].

~2 km of flood basalts were erupted rapidly across the Ethiopian Plateau at ~29–31 Ma [*Mohr*, 1983; *Hofmann et al.*, 1997] prior to or concomitant with the onset of Red Sea and Gulf of Aden rifting [e.g., *Wolfenden et al.*, 2004]. Additional shield volcanism since ~30 Ma has added a further ~2 km of local relief in regions of the Ethiopian Plateau [e.g., *Kieffer et al.*, 2004; *Beccaluva et al.*, 2009].

[7] The MER forms the third arm of the Red Sea, Gulf of Aden rift-rift-rift triple junction where the Arabian, Nubian, Somalian and Danakil Plates meet in Afar [e.g., *Wolfenden et al.*, 2004, Figure 1]. Rifting in Ethiopia began during Miocene times within the Precambrian metamorphic crustal basement of the Pan-African Mozambique belt [e.g., *Kazmin et al.*, 1978]. Extension in SW Ethiopia and northern Kenya commenced by ~20 Ma with central and northern sectors of the MER developing between ~18 and ~10 Ma, respectively [e.g., *WoldeGabriel*, 1988; *Wolfenden et al.*, 2004]. Large offset border faults formed along one or both sides of the rift (Figure 1) and are often marked by chains of silicic volcanic centers [e.g., *Chernet et al.*, 1998].

[8] Deformation in the MER north of 8.5°N is thought to have migrated to the WFB some time in the interval 6.6–3 Ma, with an associated change from 130°E directed extension to 110°E directed extension [e.g., *Wolfenden et al.*, 2004]. Geodetic data indicate that the direction of extension in the MER is N94°E at a rate of 7 mm a^{-1} [*Fernandes et al.*, 2004] and it has been proposed that ~80% of the present-day strain is localized within the MER [*Bilham et al.*, 1999]. On the strength of this evidence, *Ebinger and Casey* [2001] proposed that the extension in Ethiopia has localized since ~12 Ma, away from the Mid-Miocene border faults, toward en echelon chains of eruptive magmatic centers, dykes and small offset faults. Thus magmatic emplacement, not border faulting, increasingly dominates the rifting process after the initial stages of breakup [e.g., *Ebinger and Casey*, 2001; *Keranen et al.*, 2004; *Rooney et al.*, 2005; *Keranen and Klemperer*, 2007; *Daly et al.*, 2008; *Keranen et al.*, 2009].

[9] Much of the Quaternary magmatic activity within the MER has occurred in discrete magmatic

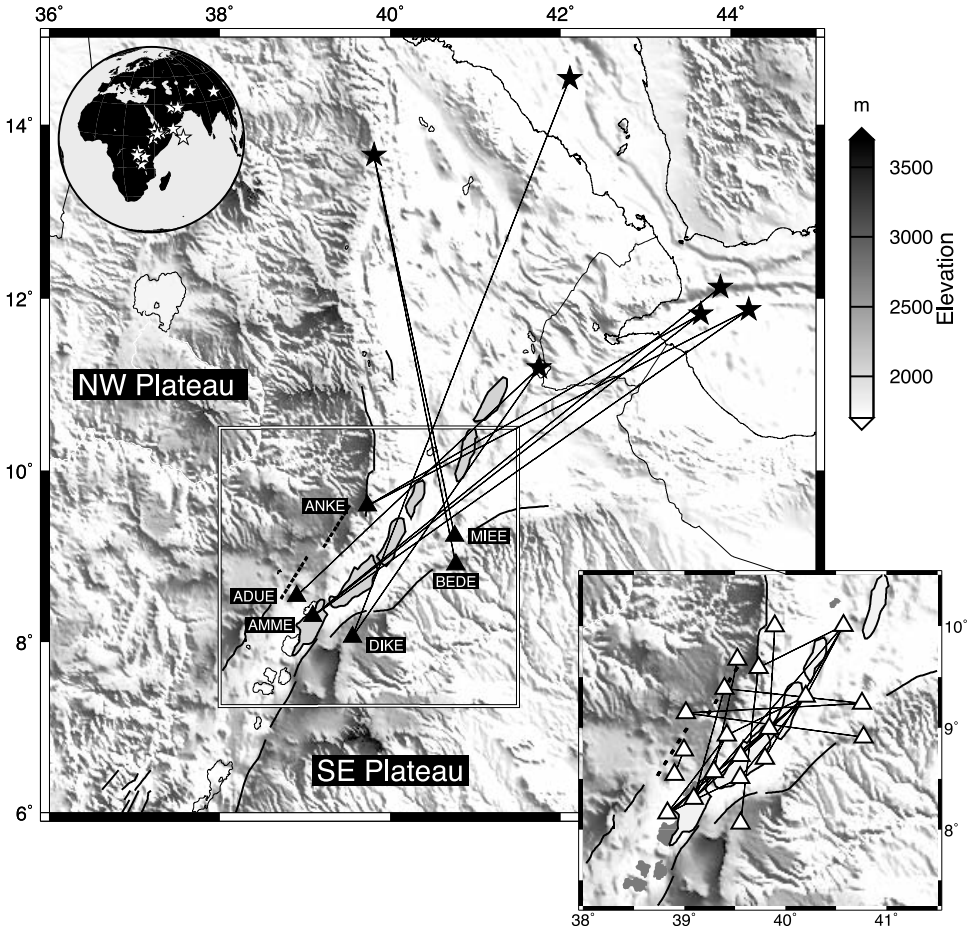

Figure 3. Paths used for group velocity dispersion measurements. Triangles and stars denote station and epicenter locations. Major Mid-Miocene border faults and Quaternary magmatic zones along the Wonjii Fault Belt (WFB) are shaded grey and delineated by the heavy black lines; dashed lines are faulted monoclines. The path characteristics are summarized in Table 2. The bottom right inset shows interstation paths used for phase velocity dispersion measurements. The station locations are denoted by the triangles and the earthquake locations are shown in the top left inset map. The interstation path characteristics are summarized in Table 3.

zones in the center of the rift in the WFB [e.g., *Mohr*, 1967; *Ebinger and Casey*, 2001], where magmas fractionate at shallow (<5 km) depths [*Rooney et al.*, 2007]. In other regions of Quaternary volcanic activity, such as the Silti Debre Zeyit Fault Zone (SDFZ, Figure 1), magma fractionation occurs at various depths throughout the ~40 km thick crust [*Rooney et al.*, 2005, 2007]. Magmatic processes in the Afar Depression and MER continue to the present day in this seismically and volcanically active rift zone [e.g., *Tadesse et al.*, 2003; *Keir et al.*, 2005; *Ayele et al.*, 2007; *Brazier et al.*, 2008; *Keir et al.*, 2009a].

2. Data

[10] Broadband seismic data come from the EAGLE passive network of 20 Güralp CMG-40TD instruments and 9 CMG-3TD instruments with nominal spacing of 40 km covering a region 250 × 350 km of the MER and its uplifted flanks (Figure 1). The network was centered on the Boset volcanic zone in the MER, ~75 km SE of Addis Ababa. Seismometers recorded at 50 s.p.s. for 16 months between October 2001 and February 2003 [e.g., *Bastow et al.*, 2005].

[11] Eighty high signal-to-noise ratio Rayleigh and Love wave seismograms were selected from 23 local, regional and teleseismic earthquakes (Table 1) recorded at 20 of the EAGLE stations (Figure 1). The seismograms from local and regional earthquakes were used to determined source-to-receiver group velocity dispersion (Figure 3); recordings from teleseismic earthquakes are used to determine interstation phase velocity dispersion. Data preparation involved deconvolution of the instrument

Table 1. Origin Times, Hypocenters, Magnitudes, and Distance Ranges of Earthquakes Used in This Study

EQ	Year	Day	Time (UT)	Latitude (deg)	Longitude (deg)	Depth (km)	Range[a] (km)	Magnitude
1	2001	318	0945:15	35.73	93.38	10	6258	5.6
2	2001	324	2108:18	−6.88	128.92	33	10050	6.3
3	2001	329	2130:54	28.32	57.27	40	2929	5.0
4	2002	009	0645:57	38.67	69.90	33	4568	5.2
5	2002	017	2001:29	−1.68	29.08	15	1579	4.7
6	2002	020	0014:44	−1.68	28.98	10	1587	5.1
7	2002	021	0439:21	−1.78	29.04	10	1590	5.1
8	2002	022	1651:00	−1.46	29.25	10	154	4.2
9	2002	027	1342:43	0.78	29.72	10	134	4.7
10	2002	048	1303:52	28.09	51.76	33	257	5.3
11	2002	051	1907:17	−7.68	31.89	39	193	5.5
12	2002	107	0847:22	27.66	56.75	33	2840	5.2
13	2002	138	1515:08	−2.91	33.73	10	1372	5.5
14	2002	169	1044:15	14.53	42.11	10	780	4.3
15	2002	181	0408:01	8.74	58.20	10	2059	5.4
16	2002	220	2117:11	13.65	40.00	15	631	4.9
17	2002	221	2208:42	11.82	43.65	15	622	5.2
18	2002	222	0945:41	12.13	43.88	15	664	4.9
19	2002	222	1556:02	13.65	39.81	15	629	5.7
20	2002	244	1715:00	14.33	51.96	10	1530	6.0
21	2002	297	0608:37	−1.82	28.98	10	1598	6.2
22	2002	324	0345:23	11.87	44.21	10	672	4.5
23	2003	001	2336:45	11.20	41.75	10	433	4.6

[a]Measured from 39.5°E, 8°N. EQ is the earthquake number.

response and rotation of the horizontal component seismograms into tangential components in order to analyze S_H for Love waves; Rayleigh waves were analyzed using the vertical component.

3. Methodology

[12] Surface wave particle motions decay with depth dependent on their wavelength. As such their velocity is period-dependent. This period dependence can thus be exploited to resolve velocity as a function of depth. Serendipitously, while Rayleigh waves are predominantly sensitive to vertical shear velocity (S_V) along the great circle path between the source and receiver [e.g., *Smith and Dahlen*, 1973], Love waves are sensitive principally to velocity tangential to the propagation direction (S_H). In tandem, therefore, *SKS*, Rayleigh and Love wave analysis can be used to resolve both depth dependence and mechanisms of seismic anisotropy [e.g., *Brisbourne et al.*, 1999].

[13] Group velocity dispersion governs energy propagation between source and receiver and therefore characterizes average Earth structure beneath the propagation path, or more precisely,

Table 2. Characteristics of the Paths for Single Station Group Velocity and Seismograms Used for Extracting the Group Velocity Dispersion[a]

N	EQ	Station	Station Latitude and Longitude (deg)	Δ_g (km)	Azimuth (deg)	Wave	Period Range (s)
1	14	DIKE	8.06, 39.56	771	22	R, L	4–26, 4–36
2	17	AMME	8.30, 39.09	633	53	R, L	4–36, 5–48
3	17	ANKE	9.59, 39.73	494	61	R	4–90
4	18	AMME	8.30, 39.09	533	52	R, L	7–36, 5–46
5	19	BEDE	8.91, 40.77	535	−8	L	6–50
6	19	MIEE	9.24, 40.76	499	−8	L	7–55
7	22	AMME	8.30, 39.09	685	55	R, L	6–50, 6–48
8	22	ANKE	9.59, 39.73	550	63	R	6–34
9	23	ADUE	8.54, 38.90	429	47	R, L	4–30, 4–24
10	23	DIKE	8.06, 39.56	422	35	R, L	6–30, 5–29

[a]Characteristics for single station group velocity are recording station, path length (Δ_g), and path azimuth, and characteristics for seismograms are surface wave type and period range. R and L denote Rayleigh and Love waves, respectively. The path azimuth is measured clockwise from north. EQ is the earthquake number, and N is the number of earthquakes.

Table 3. Characteristics of the Interstation Paths and Seismograms Used to Calculate the Interstation Phase Velocity Dispersion[a]

N	EQ	Array (km)	Δ_p (km)	Path Azimuth	Wave (s)	Periods
11	1	MEKE-GTFE	144	50	R	7–29
12	2	SENE-BEDE	194	98	R	14–41
13	3	DONE-MELE	114	39	R	10–26
14	3	MEKE-AREE	107	37	R	7–20
15	4	DONE-MELE	114	39	R	8–22
16	5	AMME-MELE	165	47	R, L	6–24, 10–22
17	6	AMME-MELE	165	47	R	6–22
18	7	AMME-MELE	165	47	R, L	7–20, 11–25
19	8	AMME-MELE	165	47	R, L	7–16, 10–20
20	9	MEKE-MELE	197	50	R	6–23
21	10	NURE-GEWE	168	30	R	8–30
22	11	MELE-GEWE	88	28	R	8–43
23	12	GEWE-AMME	250	41	R, L	11–32, 7–30
24	13	AMME-AREE	78	27	R	10–43
25	15	KOTE-MIEE	150	96	R	12–38
26	16	DZEE-ADUE	29	21	L	4–22
27	16	SHEE-GTFE	112	3	L	9–43
28	17	ANKE-GEWE	103	63	L	7–37
29	19	ANKE-DIKE	171	7	R	6–33
30	19	KOTE-AMME	125	15	R, L	4–21, 6–40
31	20	AREE-MELE	96	64	R	5–40
32	20	MEKE-DONE	88	64	R	8–37
33	21	BORE-MELE	96	47	R	6–25

[a]Characteristics of interstation paths are station pair, path length (Δ_p), and path azimuth, and characteristics of seismograms are surface wave type, surface wave mode, and period range. R and L denote Rayleigh and Love waves, respectively. The interstation path azimuth is measured clockwise from north. EQ is the earthquake number, and N is the number of earthquakes.

beneath the influence zone surrounding the propagation path. Group velocity measurements (Table 2) were thus made from local earthquake data in the cases where the propagation path was within the MER (Figure 3).

[14] Phase velocity dispersion governs the propagation speed of each harmonic component of the wave train. Earth structure was determined between the two points of phase measurements: the interstation propagation path. Data were sourced from earthquakes with a variety of epicentral distances and having interstation propagation paths covering a large range of azimuths. Figure 3 shows the earthquake locations and paths and Table 3 summarizes the measurement details. Group velocity dispersion is calculated from individual single-station paths and characterizes average Earth structure between the source and the receiver. When two or more stations lie on approximately the same great circle path to the source, phase velocity dispersion can be determined.

[15] A two-step procedure was followed to determine the path-averaged Earth models. In the first step, for a given path and a given surface wave type, the group/phase velocity dispersion was calculated for the fundamental mode data. In the second step the dispersion data were matched by inversion with a theoretical dispersion curve for a suitably chosen layered Earth. The dispersion curves are calculated and inverted separately for Rayleigh and Love waves. Fundamental mode data were used, the frequency content of which enables resolution of shallow Earth structure to ~50 km depth.

3.1. Determining Group and Phase Velocity Dispersion Curves

[16] Group velocity extraction is carried out by multiple-filter analysis [e.g., *Dziewonski et al.*, 1972]. The aim of this technique is to construct an image of the energy distribution in frequency and time and to pick the maximum energy trajectory of a surface wave mode. This is achieved by filtering the signal with a sequence of narrow band-pass Gaussian filters of different central frequencies and in each case picking the group arrival time as the largest value of the amplitude envelope. Phase match filtering is then used to improve dispersion velocity estimates, reducing the effects of spectral holes, scattered energy and lateral refraction interference.

[17] Phase velocity is extracted from two well-correlated wave trains recorded at two or more stations, when the interstation path lies very close to the great circle path. The two-station method eliminates the need for earthquake source information since the amplitude and phase source terms are common to both seismograms, and restricts the

dispersion information to the mantle structure between the two stations, rather than the entire source-station path. The extraction is achieved by stacking the seismic signal traces in the slowness period domain and locating the maxima of the stack function (R. B. Herrmann, Computer Programs in Seismology, Saint Louis University, St. Louis, Missouri, USA, 2003, available at http://www.eas.slu.edu/People/RBHerrmann/CPS330.html).

3.2. Inverting for Upper Mantle Shear Velocity

[18] In this final step, group and phase velocity dispersion curves are inverted for Earth structure. Dispersion curves from a given surface wave type are inverted simultaneously when they are associated with the same two-station paths, or different paths but with similar azimuths. Measurements 11, 16, 17, 18, 19, 20, 33 and 12, 25 (Table 3) form two such dispersion curve groups.

[19] The inversion procedure involves the minimization of the misfit between the observed phase/group velocities and those predicted from an Earth velocity model (Herrmann, Computer Programs in Seismology, 2003). The misfit is modeled as:

$$c_{\mathrm{obs}}(T_i) - c_{\mathrm{p}}(T_i) = \sum_{m=1}^{M} \frac{\partial c_{\mathrm{p}}(T_i)}{\partial \beta(z_m)}, \Delta\beta(z_m), \qquad (1)$$

where $c_{\mathrm{obs}}(T_i)$ is the observed phase/group velocity at period T_i, $c_{\mathrm{p}}(T_i)$ is the phase/group velocity predicted from the shear velocity model $\beta(z)$, $\beta(z_m)$ is the shear velocity of the mth layer, $\Delta\beta(z_m)$ is the change in $\beta(z_m)$ corresponding to $c_{\mathrm{obs}}(T_i) - c_{\mathrm{p}}(T_i)$ and M is the total number of depth layers.

[20] Equation (1) is solved iteratively for $\beta(z)$ by damped least-squares, with layers of thickness 5 km to a depth of 100 km. A choice of damping type can be made between stochastic and differential, the latter of which seeks to minimize the differences in the interlayer model changes. A combination of the two damping types was used in this study, with the smoothing constraint inhibiting the development of low-velocity zones in the final models (Herrmann, Computer Programs in Seismology, 2003). Examples of group velocity dispersion curves and interstation phase velocity curves are shown in Figures 4 and 5, respectively.

4. Results and Resolution

[21] In Figure 6, S_V and S_H are presented as a function of azimuth for depths 10 km, 20 km, 30 km, 35 km, 40 km and 45 km. At 10 km depth S_V is constantly less than S_H for all azimuths (Figure 6a). At 20 km depth (Figure 6b), the crust appears isotropic, with no consistent patterns in S_V or S_H. At depths of 30–45 km, however, different and clear patterns emerge (Figures 6c–6f). The maximum discrepancy between the two wave speeds occurs at ~35° azimuth from north, approximately the strike of the Ethiopian rift axis (Figure 1).

[22] Figure 7 shows the average resolution tensors for the S_V and S_H models shown in Figure 6. The resolution matrix maps the true model parameters into the estimated parameters and is an indication of the averaging of the true model parameters. The average resolution tensors show that velocity structure is resolved to ~50 km depth, which confirms expectations from the frequency content of the data.

[23] Factors that may have introduced artifacts and bias into the results include (1) errors arising from lateral refractions, noise and scattering, such as multiple arrivals of scattered energy; (2) the lateral averaging of the computed Earth structure due to the nature of the surface wave propagation; and (3) deviations from great circle propagation. Bias from scattering and noise was minimized by only using highly coherent wave pairs for phase velocity measurements and by applying a phase-matching filter to the data in the group velocity extraction procedure.

[24] The retrieved Earth models represent the average Earth structure within a finite zone surrounding the surface wave source-receiver or two-station path, commonly termed the "influence zone." There is, therefore, a danger of contamination of the rift valley Earth models from the surrounding plateaus. The size of the influence zone width is of some debate [e.g., *Spetzler and Snieder*, 2001; *Yoshizawa and Kennett*, 2002; *Yang and Forsyth*, 2006; *Chevrot and Zhao*, 2007], but it is generally of the order of the first Fresnel zone. The width of this zone is a function of the epicentral distance, the position on the wave path, and frequency. In particular, it increases with epicentral distance and surface wave mode rank, and it is largest at the midpoint of the source-receiver path [*Pilidou*, 2004]. Given the epicentral distances used and the frequency content of the data (period 5–50 s), the maximum width of the influence zone is not expected to exceed 50 km for models constrained by group velocity data and 80 km for models constrained by phase velocity data. The surface waves used therefore sample primarily the rift itself and significant contribution from the Earth

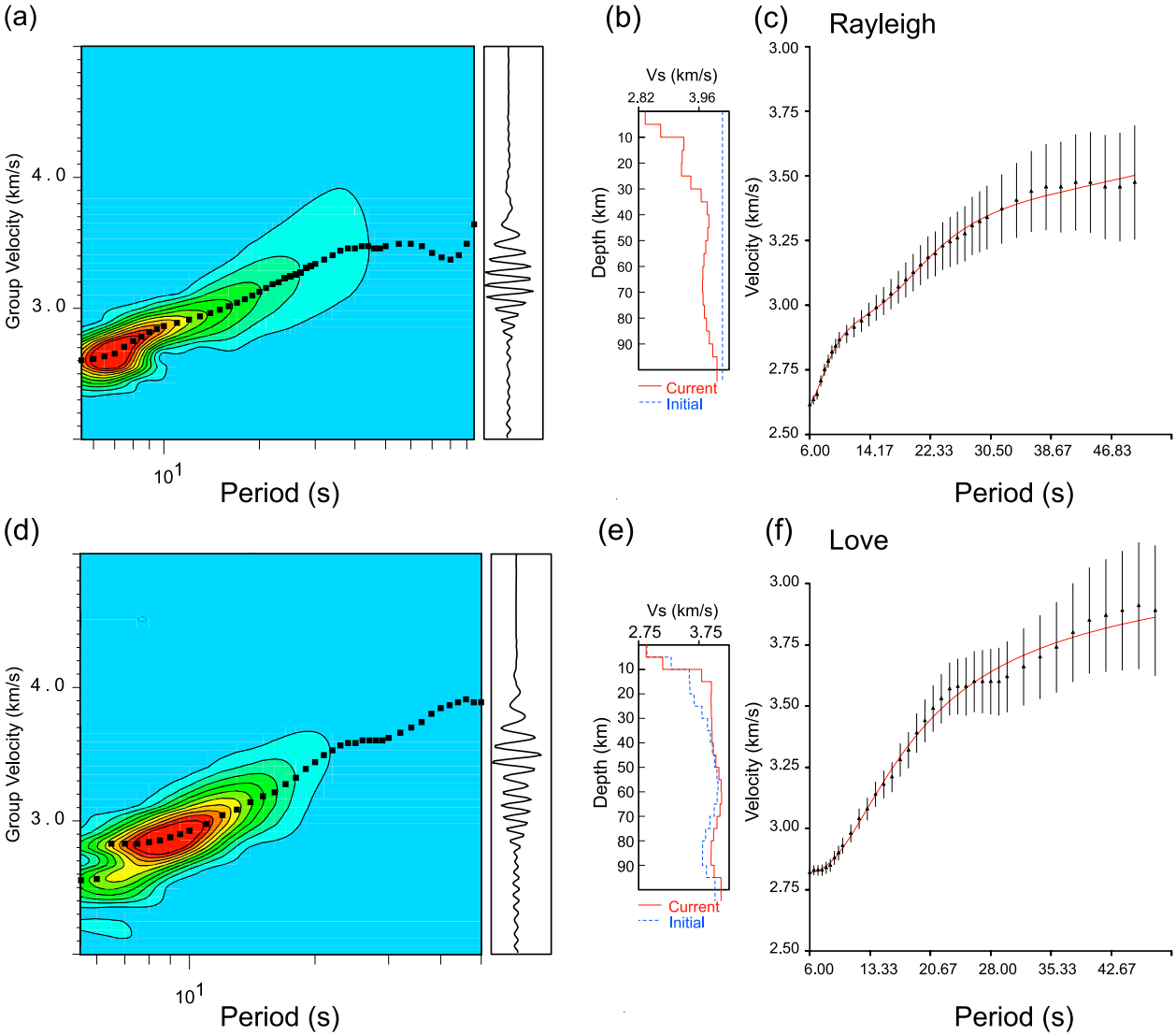

Figure 4. Example of group velocity extraction and inversion for the anisotropic Earth structure. The data, recorded at station AMME, come from local earthquake 22 (see Table 1). The path and seismogram characteristics are shown in Table 2 (measurement 7). (a) Amplitude distribution (contour lines) in the period versus group time domain for the phase-matched filtered Rayleigh waveform shown to the right of the plot. The picked curve is shown by the black triangles in Figure 4c. (b) Dispersion curve fit and (c) inverted Earth model. The red lines denote the predicted dispersion curve and the corresponding S_V wave Earth model resulting from the inversion of the dispersion data. The starting Earth model is denoted by the dashed blue line. (d–f) Same display convention as in Figures 4a–4c for the Love wave. In this case the starting Earth model for S_H is the final S_V model shown in Figures 4b and 4c.

structure beneath the surrounding plateaus of the Nubian and Somalian Plates is thus not expected.

[25] When deviation from the great circle propagation (GCP) is ignored, a systematic bias toward low velocities can be introduced in the calculated Earth models, as the assumed path length is shorter than, or in the best case equal to, the actual traveled distance, which in turn results in the underestimation of the propagation speed. Numerous studies have investigated the importance of the GCP assumption in Earth structure calculations [e.g., *Yoshizawa and Kennett*, 2002; *Ritzwoller et al.*, 2002; *Alsina and Snieder*, 1995]. The departure from the GCP is more severe when surface waves cross major geological structures such as ocean-continent boundaries, or mountain ranges and increases with decreasing period and increasing epicentral distance. Group velocity paths in this study do not pass through any major geological boundaries and are too short (Figure 3 and Table 2) for any significant effect from deviations from the

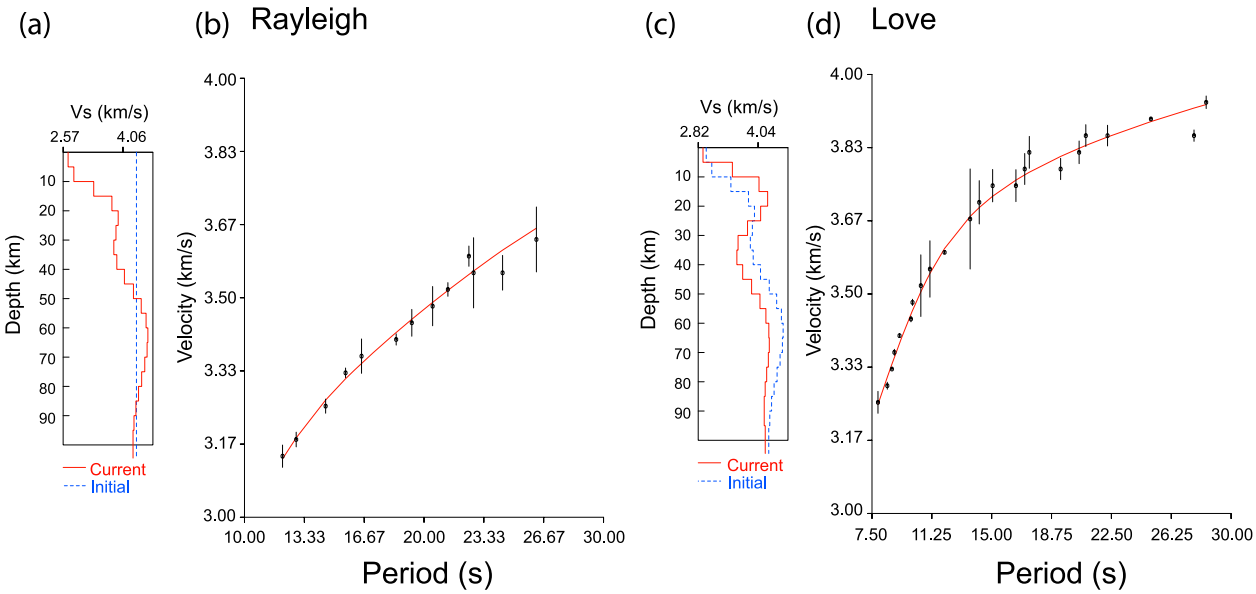

Figure 5. Interstation phase velocity dispersion curves and the inverted Earth models associated with measurement 23 (see Table 2). The data come from the recording of teleseismic earthquake 12 (see Table 1) at stations GEWE, NURE, DONE and AMME, which approximately lie on the great circle path. Rayleigh wave (a) dispersion fit and (b) inverted S_V model. Love wave (c) dispersion fit and (d) inverted S_H model. In both cases the red lines denote the Earth models and the predicted dispersion curves, whereas the error bars define the observed dispersion curves, and the dashed blue lines denote the initial shear velocity models.

GCP, despite the high frequencies used. Much longer paths were used for phase velocity measurements (Figure 3 and Table 3) that do cross major boundaries and are prone to deviations from the GCP. However, such paths are indirectly discarded by only choosing to work with highly coherent waveform pairs that do lie on the expected GCP, as in the case of severe off–great circle propagation, the two wave pairs would arrive from different points of the focal sphere, and would lose correlation. The reliability and resolution of results in the depth range 0–50 km can thus be considered good.

5. Using Seismic Anisotropy to Resolve Earth Structure

[26] The speeds of horizontally propagating S_V and S_H waves traveling through anisotropic regions vary in similar fashions with azimuth, θ, for LPO- and OMP-induced anisotropy. This variation is approximately $\cos(2\theta)$ for S_V and $\cos(4\theta)$ for S_H. However, the absolute velocity magnitudes and the difference between the two wave speed–azimuth distributions is distinctive for the two anisotropy mechanisms.

[27] Seismic anisotropy in the upper mantle is primarily caused by the LPO of olivine (and to a lesser extent enstatite) crystals in peridotite. Experimental work [e.g., *Nicolas and Christensen*, 1987; *Ismaïl and Mainprice*, 1998] and numerical simulations [e.g., *Chastel et al.*, 1993; *Blackman et al.*, 1996; *Tommasi*, 1998] show that the olivine crystal a axis [100] aligns with flow direction. This is most effective when the rock is deforming by dislocation creep, which is controlled by strain rate and history, grain size, temperature and fluid content. There is some variability in the magnitude of anisotropy observed in xenoliths of peridotite, but it is on average 5% [*Ismaïl and Mainprice*, 1998]. In general, such polycrystal rocks have triclinic elastic symmetry, but with peridotites this can be well approximated with an orthorhombic symmetry [*Blackman and Kendall*, 2002]. Anisotropy is often observed to decrease beneath 220 km [e.g., *Montagner*, 1994], possibly due to a transition from dislocation to diffusion creep, which is less effective in producing LPO [*Karato*, 1992]. More recently it has been proposed that at high pressures the dominant slip direction in olivine changes to the c axis [001], which produces little aggregate anisotropy [*Mainprice et al.*, 2005].

[28] Figures 8a–8f show P wave and S wave velocities as a function of propagation direction for a peridotite from Tanzanian upper mantle xenoliths [*Vauchez et al.*, 2005]. P wave velocities are fastest

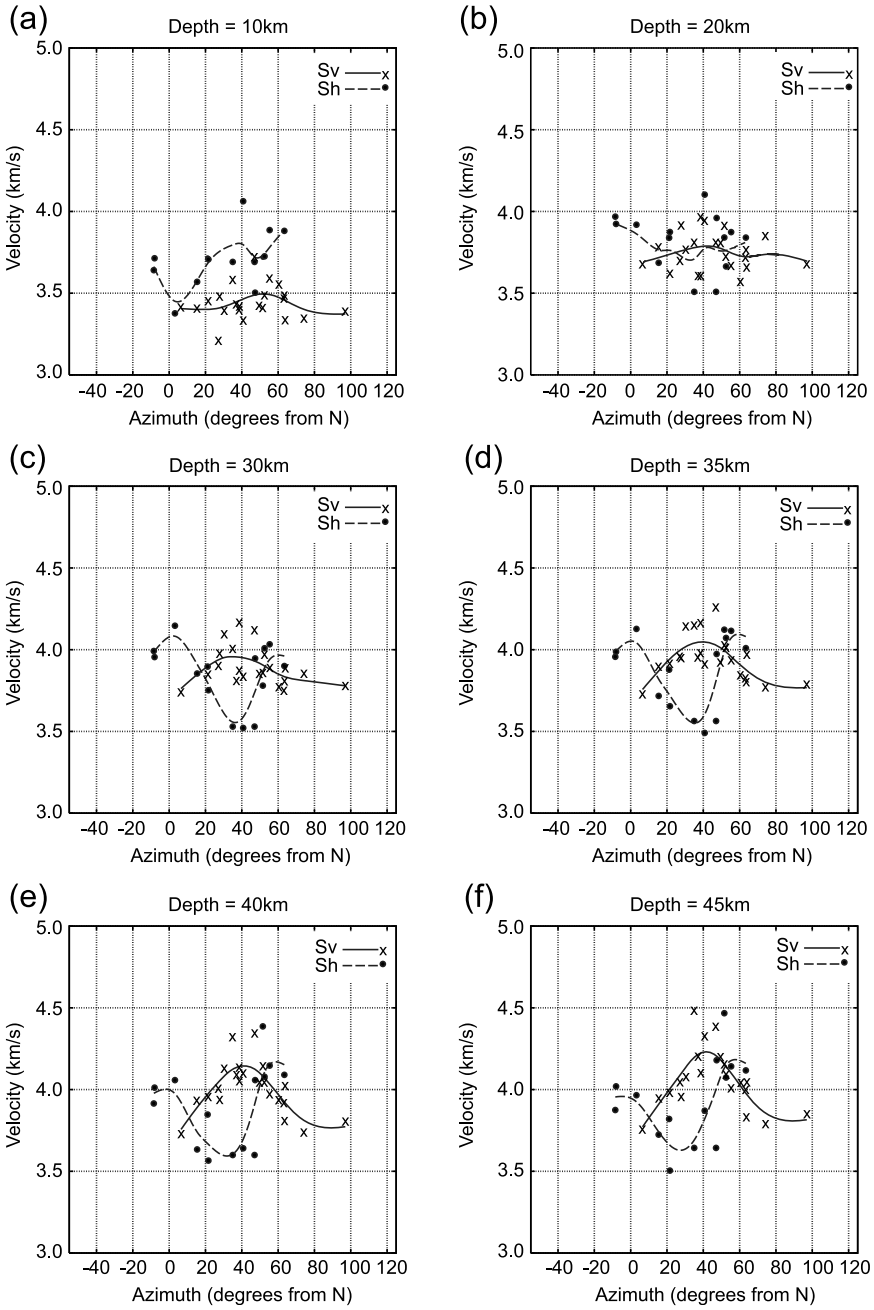

Figure 6. Azimuthal variation of the S_V and S_H wave speeds at depths of (a) 10, (b) 20, (c) 30, (d) 35, (e) 40, and (f) 45 km. The azimuth, measured clockwise from north, represents the orientation of the source-receiver path (in the case of group velocity measurements) or the interstation path (in the case of phase velocity measurements). The specific azimuth values are listed in Tables 2 and 3. In each plot, the S_V and S_H wave speed values are plotted, through which natural smoothing splines are drawn.

in the flow direction, while shear wave splitting is minimal for S wave propagation in the flow direction. With horizontal flow, a near-vertically propagating shear wave (e.g., SKS) will show large amounts of shear wave splitting and the fast shear wave will be polarized in the direction of flow. Assuming horizontal flow and horizontal wave propagation, the largest shear wave splitting will occur in directions near normal to the flow direction and horizontally polarized shear waves (S_H) will be faster than vertically polarized shear waves (S_V); consequently, Love wave analyses will yield faster shear wave models than those derived from Rayleigh waves. Love-Rayleigh models will be

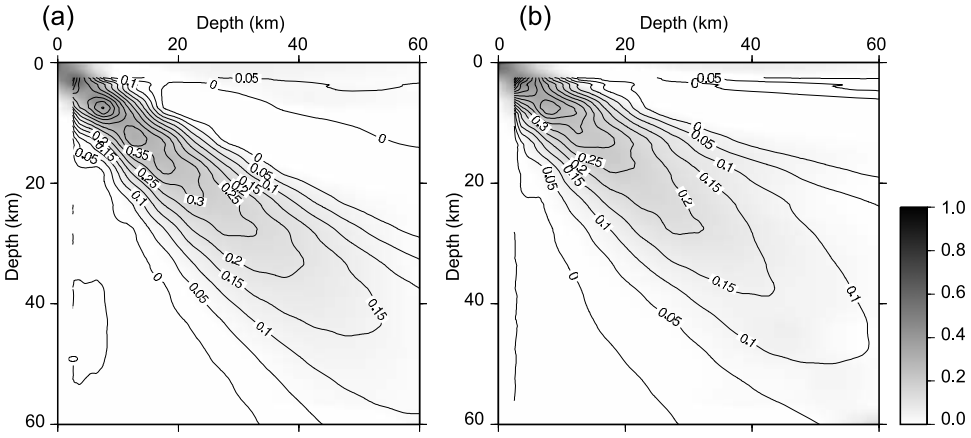

Figure 7. Average resolution tensor from all the path-averaged shear velocity models (shown in Figure 6) obtained by inverting the group and phase dispersion curves of (a) Rayleigh and (b) Love waves sampling the rift region.

more similar for surface waves propagating in the flow direction.

[29] The preferred alignment of inclusions will also produce a long-wavelength anisotropy, provided the periodicity of the inclusions is much shorter than the seismic wavelength. In contrast, LPO is a more intrinsic cause of anisotropy and will not be seismic wavelength–dependent. Microcracks vertically oriented parallel to the regional stress field are thought to be the main cause of anisotropy in the shallow crust [e.g., *Crampin*, 1994]. The resulting style of anisotropy is often referred to as azimuthal anisotropy as it produces azimuthal variations in velocities, and is often approximated by hexagonal symmetry with a horizontal symmetry axis or horizontal transverse isotropy.

[30] In addition to LPO, periodic thin layering (PTL) of materials with contrasting velocities (e.g., volcanics and sediments) can also influence aggregate seismic properties [e.g., *Valcke et al.*, 2006], and can be very effective in generating long-wavelength anisotropy [*Backus*, 1962]. If the layering is horizontal, the medium will look like a homogeneous hexagonally symmetric material with a vertical symmetry axis. This is commonly referred to as vertical transverse isotropy. Such media are distinctive because they lack azimuthal variation in velocity and do not exhibit significant shear wave splitting in vertically traveling shear waves. Thus, while body wave studies of seismic anisotropy in Ethiopia to date [*Gashawbeza et al.*, 2004; *Kendall et al.*, 2005, 2006; *Keir et al.*, 2005; *Hammond et al.*, 2010] are insensitive to PTL anisotropy, surface wave study will illuminate it as an azimuth-independent discrepancy between S_H and S_V.

[31] The preferred alignment of melt inclusions is a very effective way to generate anisotropy [e.g., *Kendall*, 1994]. The magnitude of the anisotropy is not only sensitive to the volume fraction of the melt, but to the shape of the melt inclusions as well. For example, thin disk-like inclusions are more effective in generating anisotropy than long tube-shaped inclusions [*Kendall*, 2000]. Spherical melt pockets are the least effective shapes for generating anisotropy. The shape and orientation of melt is controlled by wetting angles and strains in the medium [*Schmeling*, 1985; *Faul et al.*, 1994]. As strain and melt fraction increases, the melt will begin to align along grain edges and then melt faces.

Figure 8. Mechanisms for seismic anisotropy. (a–f) Anisotropy due to LPO of upper mantle minerals. Figure 8a shows directions of fast, slow, and medium P wave velocities, assuming a horizontal flow direction and a vertical flow plane as shown in Figure 8b. Figure 8c shows azimuthal variations in vertically and horizontally polarized shear waves (S_V versus S_H). Velocities are those determined for a peridotite from a Labait xenolith, Tanzania [*Vauchez et al.*, 2005]. Lower hemisphere pole figures show seismic velocities: P wave anisotropy is shown in Figure 8d, percent S wave splitting is shown in Figure 8e, and Figure 8f shows polarization of fast shear waves superimposed over S wave splitting contours. Flow direction is to the right, the flow plane is vertical, and the vertical direction is the center of pole figure. (g–l) Anisotropy due to OMP. Melt-induced anisotropy is modeled using theory of *Tandon and Weng* [1984] [see, e.g., *Kendall*, 2000]. Melt volume fraction is assumed to be 0.1%, and the melt lies in disk-like pockets (oblate spheroids) with an aspect ratio of 0.02. Modified after *Kendall et al.* [2006].

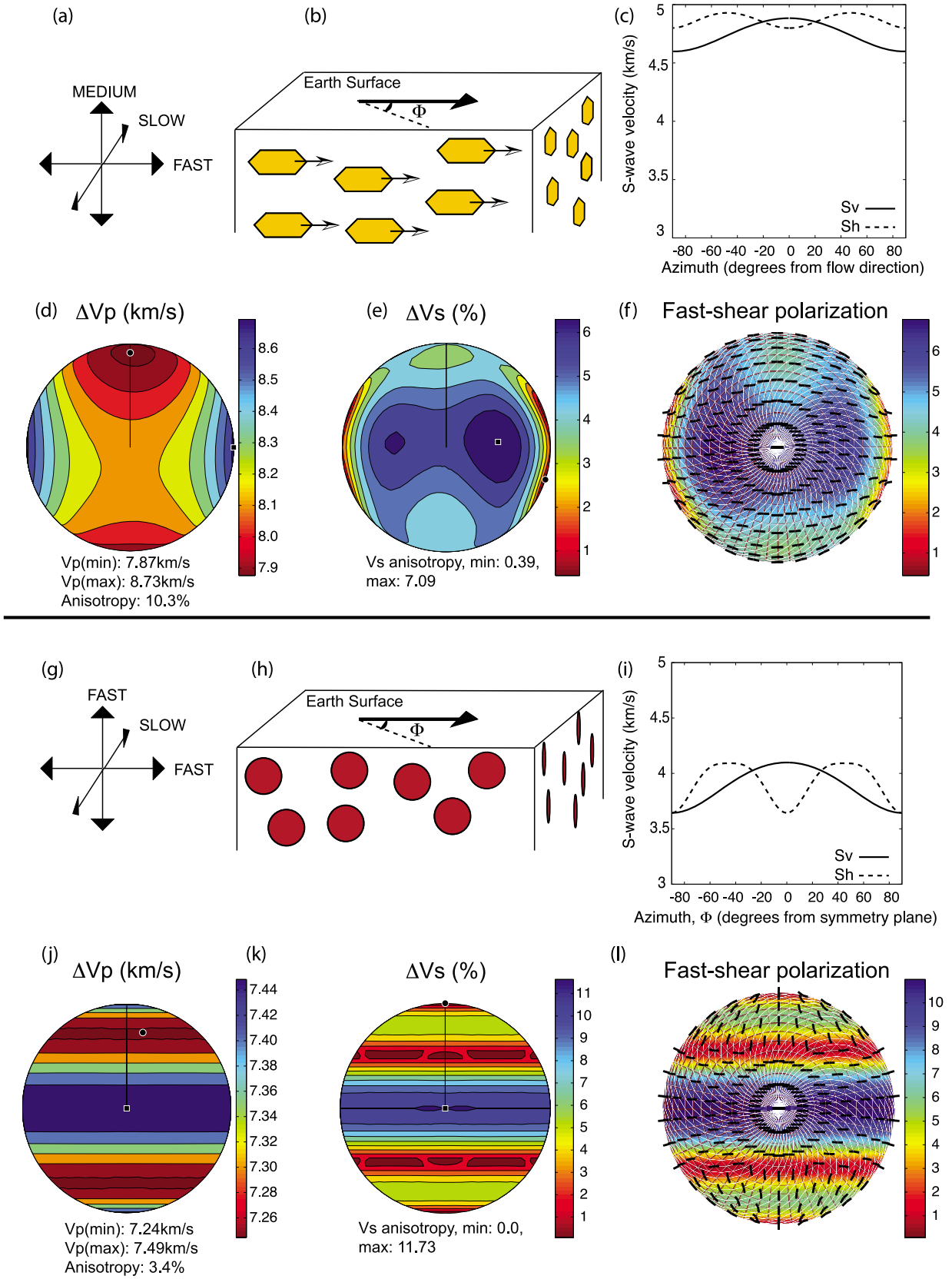
(a)
MEDIUM
SLOW
FAST
(b)
Earth Surface
Φ
(c)
S-wave velocity (km/s)
Sv
Sh
Azimuth (degrees from flow direction)
(d) ΔVp (km/s)
Vp(min): 7.87km/s
Vp(max): 8.73km/s
Anisotropy: 10.3%
(e) ΔVs (%)
Vs anisotropy, min: 0.39, max: 7.09
(f) Fast-shear polarization
(g)
FAST
SLOW
FAST
(h)
Earth Surface
Φ
(i)
S-wave velocity (km/s)
Sv
Sh
Azimuth, Φ (degrees from symmetry plane)
(j) ΔVp (km/s)
Vp(min): 7.24km/s
Vp(max): 7.49km/s
Anisotropy: 3.4%
(k) ΔVs (%)
Vs anisotropy, min: 0.0, max: 11.73
(l) Fast-shear polarization

Figure 8

[32] Figures 8g–8l show P and S wave velocities in a medium with vertically oriented melt pockets (OMP) that are tabular and disk-like in shape. Melt-induced anisotropy is modeled using theory of *Tandon and Weng* [1984] [see, e.g., *Blackman and Kendall*, 1997; *Kendall*, 2000]. Melt volume fraction is assumed to be 0.1%, and the melt lies in disk-like pockets (oblate spheroids) with an aspect ratio of 0.02. Such melt inclusions are designed to mimic the geometry of dykes that are believed to penetrate the upper crust in regions of Ethiopia where intrusions have been observed by inSar study [e.g., *Hamling et al.*, 2009; *Keir et al.*, 2009b].

[33] P wave velocities are highest for wave propagation parallel to the melt pockets, and shear wave splitting is largest in these directions. For directions of horizontal wave propagation parallel to the OMP, vertically polarized shear waves (S_V) are faster than horizontally polarized shear waves (S_H). With surface waves, Love waves would produce a slower shear wave model than that derived from Rayleigh waves. No shear wave splitting occurs when waves propagate in a direction normal to the flat face of the inclusion. These diagnostics of wave propagation in various styles of anisotropy can be used to help guide interpretations of the cause of anisotropy.

6. Discussion

6.1. Mechanisms for Anisotropy in Ethiopia

[34] Surface wave analysis has been used to gain a better understanding of the mechanisms for anisotropy beneath the MER. Results show that in the uppermost crust (Figure 6a), PTL anisotropy dominates, with $S_H > S_V$ for all sampled azimuths, consistent with field geological observations of layered basalts and sediments near the surface. Deeper in the upper crust there is little systematic variation of S_V and S_H with azimuth (Figure 6b), indicating that Pan-African basement fabric at these depths may be largely isotropic. At greater (>20 km) crustal depths, however, the nature of S_V and S_H azimuthal variations changes markedly, with S_V faster than S_H by up to 0.6 kms^{-1}, implying a ~14% anisotropic fabric. This magnitude of anisotropy in the depth range 20–90 km would predict $\delta t \approx 2.3$ s splitting in *SKS* phases, as is observed [*Kendall et al.*, 2005, 2006]. These large discrepancies between S_V and S_H are at ~35° azimuth from north, approximately the strike of the Ethiopian rift axis (Figure 1). This azimuthal maximum is consistent with predictions for OMP-induced anisotropy at depths between ~20 km and the base of the lithosphere at ~50 km (Figure 7), assuming that the ellipsoidal melt pockets are aligned parallel to the rift. Below the lithosphere, LPO anisotropic fabrics are expected to dominate [e.g., *Debayle et al.*, 2005; *Sebai et al.*, 2006; *Sicilia et al.*, 2008].

[35] The OMP hypothesis proposed here was suggested by the earlier *SKS* studies of *Ayele et al.* [2004] and *Kendall et al.* [2005, 2006], and by the local earthquake shear wave splitting study of *Keir et al.* [2005]. They noted that fast polarization directions within the MER mirror a shift from N130°E to N110°E directed extension at ~2 Ma, when surface geological studies infer that crustal strain localized toward the WFB [e.g., *Wolfenden et al.*, 2004]. While the surface wave observations of S_V and S_H could be produced by a model of vertically aligned olivine in the MER lithosphere, the large *SKS* splitting delays could not (such a fabric would predict δt close to zero). Similarly, rift parallel LPO that could explain the *SKS* observations would contradict the azimuthal variations shown in Figures 6c–6f for S_V and S_H. The present study, therefore, in conjunction with the *SKS* results, presents not only a clear case for present-day melt beneath the MER, but the mechanism by which it is incorporated into the lithosphere during breakup.

[36] The similarity of the azimuthal variations in S_V and S_H presented in Figure 6 with the OMP model presented in 8b indicate not only that a high percentage partial melt resides beneath the MER, but that it exists in low aspect ratio inclusions. Modeling of InSAR data indicates that recently intruded dykes in Ethiopia are of the order of meters wide, and kilometers long [e.g., *Keir et al.*, 2009b; *Hamling et al.*, 2009]. The anisotropic study here indicates that intrusions of similar geometry characterize the entire lithosphere below the brittle upper/middle crust.

[37] At depths greater than those analyzed in the present study, surface wave tomography indicates azimuthal anisotropy is complex beneath the region [*Debayle et al.*, 2005; *Sebai et al.*, 2006; *Sicilia et al.*, 2008]. At these depths in the upper mantle, it is likely that LPO of olivine is the dominant cause of seismic anisotropy [e.g., *Zhang and Karato*, 1995]. The LPO hypothesis at depth is consistent with regional-scale tomographic studies that image a broad (~500 km wide) low-velocity zone beneath Ethiopia that likely connects to the underlying African Superplume [e.g., *Benoit et al.*, 2006;

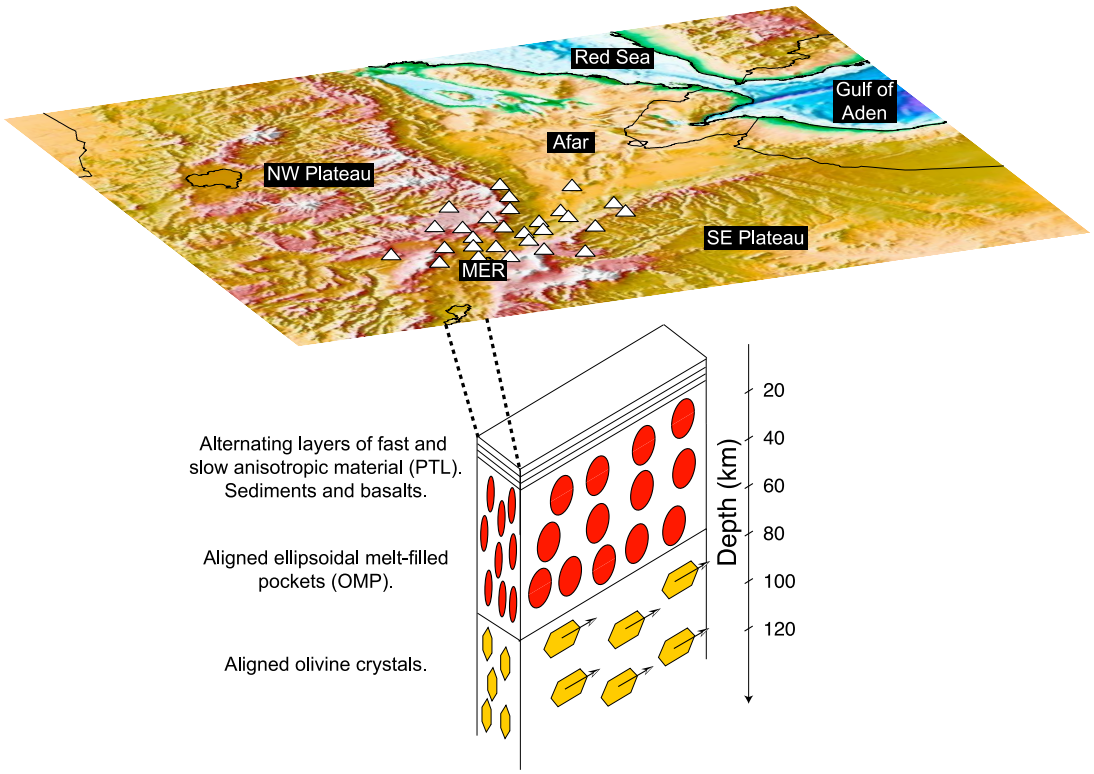

Figure 9. Suggested anisotropy mechanisms of the Ethiopian rift mantle: layering of seismically fast and slow layers in the top ~10 km and underlying OMP due to melt intrusion into the MER lithosphere. LPO in the asthenosphere due to large-scale mantle flow associated with the superplume.

Bastow et al., 2008]. Figure 9 summarizes seismic anisotropy beneath the MER.

6.2. Implications for the Evolution of Rifting

[38] The results presented here indicate the presence of melt intrusions beneath the MER to a depth of at least 50 km, but the inferred melt is not confined to the ~20 km wide WFB, the present-day locus of strain. At this latitude (~7–10°N), rifting began relatively recently (8–12 Ma [*Wolfenden et al.*, 2004]) compared to southern (~18 Ma [*WoldeGabriel et al.*, 1990]) and northern MER (~29–26 Ma [*Wolfenden et al.*, 2005]). Using $l = \sqrt{Dt}$ with $l \approx 30$ km and the thermal diffusivity $D = 1$ mm^2/s [*Turcotte and Schubert*, 1982] the time t for a significant change in thermal anomaly in the MER mantle would be ~20 Ma. Hence, thermal anomalies generated by upwelling asthenosphere since the onset of rifting in the MER have had insufficient time to decay and the effects of decompression melting beneath the entire MER are therefore expected to persist today. Elsewhere in Ethiopia (e.g., southern and central Afar) the longer period of time elapsed since the production of stretching-related decompression melts means that the asthenosphere has now had time to cool by conduction to the surface [*Bastow et al.*, 2008]. Consistent with this hypothesis, shear wave splitting delay times peak at ~7–10°N in the MER, where mantle velocities are amongst the lowest worldwide [*Bastow et al.*, 2005, 2008]. The hot, upwelling mantle beneath the MER thus provides an abundant rift-wide source of magma that is presently available for incorporation into the lithosphere during rifting.

[39] The presence of melt-filled cracks caused by magma injection reduces the strength of cold, thick lithosphere, thereby facilitating rifting when large-scale tectonic forces required to cause extension by faulting or ductile stretching of the crust may be an order of magnitude too small [*Buck*, 2004, 2006]. The OMP hypothesis is therefore consistent with time-sensitive measurements such as MT [*Whaler and Hautot*, 2006], seismicity studies [*Keir et al.*, 2009a] and geochemical studies of MER Quaternary magma genesis [*Rooney et al.*, 2005, 2007]

that all suggest ongoing dyke intrusion is accommodating extension in the MER, without marked crustal thinning [*Dugda et al.*, 2005; *Stuart et al.*, 2006; *Cornwell et al.*, 2010].

7. Conclusions

[40] Group velocity and interstation phase velocity measurements from both local and teleseismic earthquakes have been used to constrain mechanisms of seismic anisotropy in the crust and upper mantle beneath the Ethiopian rift. Three mechanisms are identified: (1) Periodic thin layering (PTL) anisotropy in the uppermost crust characterizes the sediments and basalt flows near the surface. (2) Between ~20 and ~50 km depth surface wave results, in conjunction with existing studies of *SKS* shear wave splitting in the MER, indicate that oriented melt pocket (OMP) type anisotropy dominated the observations. (3) At greater depths in the mantle, anisotropy is caused by olivine LPO. These conclusions are summarized in Figure 9. These results confirm that previously reported zones of dense, seismically fast, and partially molten zones of intrusion in the MER crust are composed of low aspect ratio melt inclusions (dykes and veins). The MER is thus a type example of an active magma assisted rift and our results join a growing body of evidence from rift settings worldwide that now recognize the importance of magma intrusion during breakup. Such observations have significant implications for the improved estimation of stretching factors and the thermal evolution of potentially hydrocarbon-rich passive margins.

Acknowledgments

[41] We thank R. Herrmann for making public his computer code and Andrea Tommasi for providing elastic constants for peridotites. Stewart Fishwick provided helpful advice that improved the quality of the manuscript. Laike Asfaw, Atalay Ayele, and their colleagues at Addis Ababa University are thanked for their support throughout the course of our experiments in Ethiopia. Comments from Joel Baker, Christel Tiberi, and an anonymous reviewer improved the clarity of the manuscript. The EAGLE project was supported by NERC grant NER/A/S/2000/01003.

References

Alsina, D., and R. Snieder (1995), Small-scale sublithospheric mantle deformation: Constraints from SKS splitting observations, *Geophys. J. Int.*, *123*, 431–448.

Ayele, A., G. W. Stuart, and J.-M. Kendall (2004), Insights into rifting from shear wave splitting and receiver functions: An example from Ethiopia, *Geophys. J. Int.*, *157*, 354–362.

Ayele, A., G. W. Stuart, I. D. Bastow, and D. Keir (2007), The August 2002 earthquake sequence in north Afar: Insights into the neotectonics of the Danakil microplate, *J. Afr. Earth Sci.*, *40*, 70–79.

Backus, G. (1962), Long-wave elastic anisotropy produced by horizontal layering, *J. Geophys. Res.*, *67*, 4427–4440.

Bastow, I. D., G. W. Stuart, J.-M. Kendall, and C. J. Ebinger (2005), Upper-mantle seismic structure in a region of incipient continental breakup: Northern Ethiopian rift, *Geophys. J. Int.*, *162*, 479–493.

Bastow, I. D., T. J. Owens, G. Helffrich, and J. H. Knapp (2007), Spatial and temporal constraints on sources of seismic anisotropy: Evidence from the Scottish highlands, *Geophys. Res. Lett.*, *34*, L05305, doi:10.1029/2006GL028911.

Bastow, I. D., A. A. Nyblade, G. W. Stuart, T. O. Rooney, and M. H. Benoit (2008), Upper mantle seismic structure beneath the Ethiopian hot spot: Rifting at the edge of the African low-velocity anomaly, *Geochem. Geophys. Geosyst.*, *9*, Q12022, doi:10.1029/2008GC002107.

Bastow, I. D., D. Keir, and E. Daly (2010), The Ethiopia Afar Geoscientific Lithospheric Experiment (EAGLE): Probing the transition from continental rifting to incipient sea floor spreading, *Spec. Pap. Geol. Soc. Am.*, in press.

Beccaluva, L., G. Bianchini, C. Natali, and F. Siena (2009), Continental flood basalts and mantle plumes: A case study of the Northern Ethiopian Plateau, *J. Petrol.*, *50*, 1377–1403, doi:10.1093/petrology/egp024.

Benoit, M. H., A. A. Nyblade, and J. C. VanDecar (2006), Upper mantle *P* wavespeed variations beneath Ethiopia and the origin of the Afar hotspot, *Geology*, *34*(5), 329–332.

Bilham, R., R. Bendick, K. Larson, P. Mohr, J. Braun, S. Tesfaye, and L. Asfaw (1999), Secular and tidal strain across the Main Ethiopian Rift, *Geophys. Res. Lett.*, *26*, 2789–2792.

Blackman, D., and J. M. Kendall (1997), Sensitivity of teleseismic body waves to mineral texture and melt in the mantle beneath a mid–ocean ridge, *Philos. Trans. R. Soc. London*, *355*, 217–231.

Blackman, D. K., and J.-M. Kendall (2002), Seismic anisotropy in the upper mantle 2. Predictions for current plate boundary flow models, *Geochem. Geophys. Geosyst.*, *3*(9), 8602, doi:10.1029/2001GC000247.

Blackman, D. K., J. M. Kendall, P. R. Dawson, H. R. Wenk, D. Boyce, and J. P. Morgan (1996), Teleseismic imaging of subaxial flow at mid-ocean ridges: Travel-time effects of anisotropic mineral texture in the mantle, *Geophys. J. Int.*, *127*(2), 415–426.

Brazier, R. A., Q. Miao, A. A. Nyblade, A. Ayele, and C. A. Langston (2008), Local magnitude scale for the Ethiopian Plateau, *Bull. Seismol. Soc. Am.*, *98*(5), 2341–2348, doi:10.1785/0120070266.

Brisbourne, A., G. Stuart, and J.-M. Kendall (1999), Anisotropic structure of the Hikurangi subduction zone, New Zealand—Integrated interpretation of surface-wave and body-wave observations, *Geophys. J. Int.*, *137*(1), 214–230.

Buck, W. R. (2004), Consequences of asthenospheric variability on continental rifting, in *Rheology and Deformation of the Lithosphere at Continental Margins*, edited by G. Karner et al., pp. 1–30, Columbia Univ. Press, New York.

Buck, W. R. (2006), The role of magma in the development of the Afro-Arabian Rift System, in *The Structure and Evolution of the East African Rift System in the Afar Volcanic*

Province, edited by G. Yirgu, C. J. Ebinger, and P. K. H. Maguire, *Geol. Soc. Spec. Publ.*, *259*, 43–54.

Chastel, Y. B., P. R. Dawson, H. R. Wenk, and K. Bennett (1993), Anisotropic convection with implications for the upper mantle, *J. Geophys. Res.*, *98*(B10), 17,757–17,771.

Chernet, T., W. K. Hart, J. L. Aronson, and R. C. Walter (1998), New age constraints on the timing of volcanism and tectonism in the northern Main Ethiopian Rift—Southern Afar transition zone (Ethiopia), *J. Volcanol. Geotherm. Res.*, *80*, 267–280.

Chevrot, S., and L. Zhao (2007), Multi-scale finite-frequency Rayleigh wave tomography of the Kaapvaal craton, *Geophys. J. Int.*, *169*(1), 201–215.

Coffin, M. F., and O. Eldholm (1994), Large igneous provinces: Crustal structure, dimensions, and external consequences, *Rev. Geophys*, *32*(1), 1–36.

Cornwell, D. G., G. D. Mackenzie, R. W. England, P. K. H. Maguire, L. M. Asfaw, and B. Oluma (2006), Northern Main Ethiopian Rift crustal structure from new high-precision gravity data, in *The Afar Volcanic Province Within the East African Rift System*, edited by G. Yirgu, C. J. Ebinger, and P. K. H. Maguire, *Geol. Soc. Spec. Publ.*, *256*, 309–323.

Cornwell, D. G., P. K. H. Maguire, R. W. England, and G. W. Stuart (2010), Imaging detailed crustal structure and magmatic intrusion across the Ethiopian Rift using a dense linear broadband array, *Geochem. Geophys. Geosyst.*, *11*, Q0AB03, doi:10.1029/2009GC002637.

Corti, G. (2008), Control of rift obliquity on the evolution and segmentation of the main Ethiopian rift, *Nat. Geosci.*, *1*(4), 258–262.

Crampin, S. (1994), The fracture criticality of crustal rocks, *Geophys. J. Int.*, *118*, 428–438.

Daly, E., D. Keir, C. J. Ebinger, G. W. Stuart, I. D. Bastow, and A. Ayele (2008), Crustal tomographic imaging of a transitional continental rift: The Ethiopian rift, *Geophys. J. Int.*, *172*(3), 1033–1048.

Debayle, E., J. J. Lévêque, and M. Cara (2001), Seismic evidence for a deeply rooted low-velocity anomaly in the upper mantle beneath the northeastern Afro/Arabian continent, *Earth Planet. Sci. Lett.*, *193*, 423–436.

Debayle, E., B. Kennett, and K. Priestley (2005), Global azimuthal seismic anisotropy and the unique plate-motion deformation of Australia, *Nature*, *433*(7025), 509–512.

Dugda, M. T., A. A. Nyblade, J. Julia, C. A. Langston, C. J. Ammon, and S. Simiyu (2005), Crustal structure in Ethiopia and Kenya from receiver function analysis: Implications for rift development in eastern Africa, *J. Geophys. Res.*, *110*, B01303, doi:10.1029/2004JB003065.

Dugda, M. T., A. A. Nyblade, and J. Julià (2007), Thin lithosphere beneath the Ethiopian plateau revealed by a joint inversion of Rayleigh wave group velocities and receiver functions, *J. Geophys. Res.*, *112*, B08305, doi:10.1029/2006JB004918.

Dziewonski, A., J. Mills, and S. Bloch (1972), Residual dispersion measurement—A new method of surface-wave analysis, *Bull. Seismol. Soc. Am.*, *62*(1), 129–139.

Ebinger, C. E. (2005), Continental break-up: The East African perspective, *Astron. Geophys.*, *46*, 16–21.

Ebinger, C. E., and M. Casey (2001), Continental breakup in magmatic provinces: An Ethiopian example, *Geology*, *29*, 527–530.

Ebinger, C. E., T. Yemane, G. WoldeGabriel, J. Aronson, and R. Walter (1993), Eocene-Recent volcanism and faulting in the southern Main Ethiopian rift, *J. Geol. Soc. London*, *150*, 99–108.

Faul, U. H., D. R. Toomey, and H. S. Waff (1994), Intergranular basaltic melt is distributed in thin, elogated inclusions, *Geophys. Res. Lett.*, *21*(1), 29–32.

Fernandes, R. M. S., B. A. C. Ambrousius, R. Noomen, L. Bastos, L. Combrinck, J. M. Miranda, and W. Spakman (2004), Angular velocities of Nubia and Somalia from continuous GPS data: Implications on present-day relative kinematics, *Earth Planet. Sci. Lett.*, *222*, 197–208.

Furman, T., J. Bryce, B. Hanan, G. Yirgu, and D. Ayalew (2006), Heads and tails: 30 years of the Afar plume, in *The Afar Volcanic Province within the East African Rift System*, edited by G. Yirgu, C. J. Ebinger, and P. K. H. Maguire, *Geol. Soc. Spec. Publ.*, *259*, 95–119.

Gashawbeza, E. M., S. L. Klemperer, A. A. Nyblade, K. T. Walker, and K. M. Keranen (2004), Shear-wave splitting in Ethiopia: Precambrian mantle anisotropy locally modified by Neogene rifting, *Geophys. Res. Lett.*, *31*, L18602, doi:10.1029/2004GL020471.

George, R., N. Rogers, and S. Kelley (1998), Earliest magmatism in Ethiopia: Evidence for two mantle plumes in one continental flood basalt province, *Geology*, *26*, 923–926.

Grand, S. P. (2002), Mantle shear-wave tomography and the fate of subducted slabs, *Philos. Trans. R. Soc. London, Ser. A*, *360*, 2475–2491.

Hamling, I. J., A. Ayele, L. Bennati, E. Calais, C. J. Ebinger, D. Keir, E. Lewi, T. J. Wright, and G. Yirgu (2009), Geodetic observations of the ongoing Dabbahu rifting episode: New dyke intrusions in 2006 and 2007, *Geophys. J. Int.*, *178*, 989–1003, doi:10.1111/j.1365-246X.2009.04163.x.

Hammond, J. O. S., J.-M. Kendall, D. Angus, and J. Wookey (2010), Interpreting spatial variations in anisotropy: Insights into the Main Ethiopian Rift from SKS waveform modelling, *Geophys. J. Int.*, in press.

Hofmann, C., V. Courtillot, G. Feraud, P. Rochette, G. Yirgu, E. Ketefo, and R. Pik (1997), Timing of the Ethiopian flood basalt event and implications for plume birth and global change, *Nature*, *389*, 838–841.

Ismaïl, W. B., and D. Mainprice (1998), An olivine fabric database: An overview of upper mantle fabrics and seismic anisotropy, *Tectonophysics*, *296*(1–2), 145–157.

Karato, S. (1992), On the Lehmann discontinuity, *Geophys. Res. Lett.*, *19*(22), 2255–2258.

Kazmin, V., A. Shifferaw, and T. Balcha (1978), The Ethiopian basement: Stratigraphy and possible manner of evolution, *Geol. Rundsch.*, *67*, 531–546.

Keir, D., J.-M. Kendall, C. J. Ebinger, and G. W. Stuart (2005), Variations in late syn-rift melt alignment inferred from shear-wave splitting in crustal earthquakes beneath the Ethiopian rift, *Geophys. Res. Lett.*, *32*, L23308, doi:10.1029/2005GL024150.

Keir, D., I. D. Bastow, K. A. Whaler, E. Daly, D. G. Cornwell, and S. Hautot (2009a), Lower crustal earthquakes near the Ethiopian rift induced by magmatic processes, *Geochem. Geophys. Geosyst.*, *10*, Q0AB02, doi:10.1029/2009GC002382.

Keir, D., et al. (2009b), Evidence for focused magmatic accretion at segment centers from lateral dike injections captured beneath the Red Sea rift in Afar, *Geology*, *37*(1), 979–982.

Kendall, J.-M. (1994), Teleseismic arrivals at a mid-ocean ridge: Effects of melt and anisotropy, *Geophys. Res. Lett.*, *21*, 301–304.

Kendall, J.-M. (2000), Seismic anisotropy in the boundary layers of the mantle, in *Earth's Deep Interior, Mineral Physics and Tomography From the Atomic to the Global Scale*, *Geophys. Monogr. Ser.*, vol. 117, edited by S. Karato et al., pp. 149–175, AGU, Washington, D. C.

Kendall, J.-M., G. W. Stuart, C. J. Ebinger, I. D. Bastow, and D. Keir (2005), Magma assisted rifting in Ethiopia, *Nature*, *433*, 146–148.

Kendall, J.-M., S. Pilidou, D. Keir, I. D. Bastow, G. W. Stuart, and A. Ayele (2006), Mantle upwellings, melt migration and the rifting of Africa: Insights from seismic anisotropy, in *The Afar Volcanic Province Within the East African Rift System*, edited by G. Yirgu, C. J. Ebinger, and P. K. H. Maguire, *Geol. Soc. Spec. Publ.*, *259*, 55–72.

Keranen, K., and S. L. Klemperer (2007), Discontinuous and diachronous evolution of the Main Ethiopian Rift: Implications for development of continental rifts, *Earth Planet. Sci. Lett.*, *265*, 96–111.

Keranen, K., S. L. Klemperer, R. Gloaguen, and EAGLE Working Group (2004), Three-dimensional seismic imaging of a protoridge axis in the main Ethiopian rift, *Geology*, *32*, 949–952.

Keranen, K. M., S. L. Klemperer, J. Julia, J. F. Lawrence, and A. A. Nyblade (2009), Low lower crustal velocity across Ethiopia: Is the Main Ethiopian Rift a narrow rift in a hot craton?, *Geochem. Geophys. Geosyst.*, *10*, Q0AB01, doi:10.1029/2008GC002293.

Kieffer, B., et al. (2004), Flood and shield basalts from Ethiopia: Magmas from the African Superswell, *J. Petrol.*, *45*(4), 793–834.

Knox, R. P., A. A. Nyblade, and C. A. Langston (1998), Upper mantle S velocities beneath Afar and western Saudi Arabia from Rayleigh wave dispersion, *Geophys. Res. Lett.*, *25*, 4233–4236.

Li, C., R. D. van der Hilst, E. R. Engdahl, and S. Burdick (2008), A new global model for P wave speed variations in Earth's mantle, *Geochem. Geophys. Geosyst.*, *9*, Q05018, doi:10.1029/2007GC001806.

Mackenzie, G. D., H. Thybo, and P. K. H. Maguire (2005), Crustal velocity structure across the Main Ethiopian Rift: Results from 2-dimensional wide-angle seismic modelling, *Geophys. J. Int.*, *162*, 994–1006, doi:10.1111/j.1365–246X.2005.02710.x.

Maguire, P. K. H., G. R. Keller, S. L. Klemperer, G. D. Mackenzie, S. Harder, B. O'Reilly, H. Thybo, L. Asfaw, M. A. Khan, and M. Amha (2006), Crustal structure of the northern Main Ethiopian Rift from the EAGLE controlled-source survey: A snapshot of incipient lithospheric break-up, in *The Afar Volcanic Province Within the East African Rift System*, edited by G. Yirgu, C. J. Ebinger, and P. K. H. Maguire, *Geol. Soc. Spec. Publ.*, *259*, 271–293.

Mainprice, D., A. Tommasi, H. Couvy, P. Cordier, and D. J. Frost (2005), Pressure sensitivity of olivine slip systems and seismic anisotropy of Earth's upper mantle, *Nature*, *433*(7027), 731–733.

Maresh, J., and R. S. White (2005), Seeing through a glass, darkly: Strategies for imaging through basalt, *First Break*, *23*, 27–33.

Menzies, M., S. Klemperer, C. Ebinger, and J. Baker (2002), Characteristics of volcanic rifted margins, volcanic rifted margins, *Spec. Pap. Geol. Soc. Am.*, *362*, 1–14.

Mickus, K., K. Tadesse, G. R. Keller, and B. Oluma (2007), Gravity analysis of the main Ethiopian rift, *J. Afr. Earth Sci.*, *48*(2–3), 59–69.

Mohr, P. A. (1967), Major volcanotectonic lineament in the Ethiopian rift system, *Nature*, *213*, 664–665.

Mohr, P. A. (1983), Ethiopian flood basalt province, *Nature*, *303*, 577–584.

Montagner, J. P. (1994), Can seismology tell us anything about convection in the mantle?, *Rev. Geophys.*, *32*(2), 115–137.

Montelli, R., G. Nolet, F. A. Dahlen, and G. Masters (2006), A catalogue of deep mantle plumes: New results from finite-frequency tomography, *Geochem. Geophys. Geosyst.*, *7*, Q11007, doi:10.1029/2006GC001248.

Nicolas, A., and N. I. Christensen (1987), Formation of anisotropy in upper mantle peridotites—A review, in *Composition, Structure and Dynamics of the Lithosphere-Asthenosphere System*, *Geodyn. Ser.*, vol. 16, edited by K. Fuchs and C. Froidevaux, pp. 111–123, AGU, Washington, D. C.

Nielsen, C., and H. Thybo (2009), Lower crustal intrusions beneath the southern Baikal Rift Zone: Evidence from full-waveform modelling of wide-angle seismic data, *Tectonophysics*, *470*(3–4), 298–318.

Pasyanos, M. E., and A. A. Nyblade (2007), A top to bottom lithospheric study of Africa and Arabia, *Tectonophysics*, *444*(1–4), 27–44.

Pilidou, S. (2004), Upper mantle shear-wave velocity and anisotropy structure beneath the North Atlantic: A seismic image of the Iceland mantle plume, Ph.D. thesis, Cambridge Univ., Cambridge, U. K.

Priestley, K., D. McKenzie, E. Debayle, and S. Pilidou (2008), The African upper mantle and its relationship to tectonics and surface geology, *Geophys. J. Int.*, *175*(3), 1108–1126.

Ritsema, J., and H. van Heijst (2000), New seismic model of the upper mantle beneath Africa, *Geology*, *28*(1), 63–66.

Ritzwoller, M. H., N. M. Shapiro, M. P. Barmin, and A. L. Levshin (2002), Global surface wave diffraction tomography, *J. Geophys. Res.*, *107*(B12), 2335, doi:10.1029/2002JB001777.

Rooney, T. O. (2010), Geochemical evidence of lithospheric thinning in the southern Main Ethiopian Rift, *Lithos*, doi:10.1016/j.lithos.2010.02.002, in press.

Rooney, T. O., T. Furman, G. Yirgu, and D. Ayalew (2005), Structure of the Ethiopian lithosphere: Xenolith evidence in the Main Ethiopian Rift, *Geochim. Cosmochim. Acta*, *69*(15), 3889–3910, doi:10.1016/j.gca.2005.03.043.

Rooney, T., T. Furman, I. Bastow, D. Ayalew, and G. Yirgu (2007), Lithospheric modification during crustal extension in the Main Ethiopian Rift, *J. Geophys. Res.*, *112*, B10201, doi:10.1029/2006JB004916.

Schmeling, H. (1985), Numerical models on the influence of partial melt on elastic, anelastic and electric properties of rocks. Part I: Elasticity and anelasticity, *Phys. Earth Planet. Inter.*, *41*(1), 34–57.

Sebai, A., E. Stutzmann, J. P. Montagner, D. Sicilia, and E. Beucler (2006), Anisotropic structure of the African upper mantle from Rayleigh and Love wave tomography, *Phys. Earth Planet. Inter.*, *155*(1–2), 48–62.

Sicilia, D., et al. (2008), Upper mantle structure of shear-waves velocities and stratification of anisotropy in the Afar Hotspot region, *Tectonophysics*, *462*(1–4), 164–177.

Simmons, N. A., A. M. Forte, and S. P. Grand (2007), Thermochemical structure and dynamics of the African superplume, *Geophys. Res. Lett.*, *34*, L02301, doi:10.1029/2006GL028009.

Smith, M. L., and F. A. Dahlen (1973), Azimuthal dependence of love and rayleigh wave propagation in a slightly anisotropic medium, *J. Geophys. Res.*, *78*(17), 3321–3333.

Spetzler, J., and R. Snieder (2001), The effect of small-scale heterogeneity on the arrival time of waves, *Geophys. J. Int.*, *145*, 786–796.

Stuart, G. W., I. D. Bastow, and C. J. Ebinger (2006), Crustal structure of the northern Main Ethiopian rift from receiver function studies, in *The Afar Volcanic Province Within the East African Rift System*, edited by G. Yirgu, C. J. Ebinger, and P. K. H. Maguire, *Geol. Soc. Spec. Publ.*, *259*, 271–293.

Tadesse, S., J.-P. Milesi, and Y. Deschamps (2003), Geology and mineral potential of Ethiopia: A note on geology and mineral map of Ethiopia, *J. Afr. Earth Sci.*, *36*, 273–313.

Tandon, G. P., and G. J. Weng (1984), The effect of aspect ratio of inclusions on the elastic properties of unidirectionally aligned composites, *Polymer Composites*, *5*, 327–333.

Thybo, H., and C. A. Nielsen (2009), Magma-compensated crustal thinning in continental rift zones, *Nature*, *457* (7231), 873–876.

Tiberi, C., C. Ebinger, V. Ballu, G. W. Stuart, and B. Oluma (2005), Inverse models of gravity data from the Red Sea-Aden-East African rifts triple junction zone, *Geophys. J. Int.*, *163*(2), 775–787.

Tommasi, A. (1998), Forward modeling of the development of seismic anisotropy in the upper mantle, *Earth Planet. Sci. Lett.*, *160*(1–2), 1–13.

Turcotte, D. L., and G. Schubert (1982), *Geodynamics Applications of Continuum Physics to Geological Problems*, 450 pp., John Wiley, New York.

Valcke, S. L. A., M. Casey, G. E. Lloyd, J. M. Kendall, and Q. J. Fisher (2006), Lattice preferred orientation and seismic anisotropy in sedimentary rocks, *Geophys. J. Int.*, *166*(2), 652–666.

Vauchez, A., F. Dineur, and R. Rudnick (2005), Microstructure, texture and seismic anisotropy of the lithospheric mantle: Insights from the Labait volcano xenoliths (Tanzania), *Earth Planet. Sci. Lett.*, *232*, 295–314.

Whaler, K. A., and S. Hautot (2006), The electrical resistivity structure of the crust beneath the northern Ethiopian rift, in *The Afar Volcanic Province Within the East African Rift System*, edited by G. Yirgu, C. J. Ebinger, and P. K. H. Maguire, *Geol. Soc. Spec. Publ.*, *256*, 293–305.

White, R. S., and L. K. Smith (2009), Crustal structure of the Hatton and the conjugate east Greenland rifted volcanic continental margins, NE Atlantic, *J. Geophys. Res.*, *114*, B02305, doi:10.1029/2008JB005856.

White, R. S., L. K. Smith, A. W. Roberts, P. A. F. Christie, N. J. Kusznir, and the rest of the iSIMM Team (2008), Lower-crustal intrusion on the North Atlantic continental margin, *Nature*, *452*(7186), 460–464.

WoldeGabriel, G. (1988), Volcanotectonic history of the central sector of the main Ethiopian rift: A geochronological, geochemical and petrological approach, Ph.D. thesis, Case Western Reserve Univ., Cleveland, Ohio.

WoldeGabriel, G., J. L. Aronson, and R. C. Walter (1990), Geology, geochronology, and rift basin development in the central sector of the Main Ethiopia Rift, *Geol. Soc. Am. Bull.*, *102*(4), 439–458.

Wolfenden, E., C. J. Ebinger, G. Yirgu, A. Deino, and D. Ayalew (2004), Evolution of the northern main Ethiopian rift: Birth of a triple junction, *Earth Planet. Sci. Lett.*, *224*, 213–228.

Wolfenden, E., C. J. Ebinger, G. Yirgu, P. Renne, and S. P. Kelley (2005), Evolution of a volcanic rifted margin: Southern Red Sea, Ethiopia, *Geol. Soc. Am. Bull.*, *117*(7–8), 846–864.

Yang, Y., and D. W. Forsyth (2006), Regional tomographic inversion of the amplitude and phase of Rayleigh waves with 2-D sensitivity kernels, *Geophys. J. Int.*, *166*(3), 1148–1160.

Yoshizawa, K., and B. L. N. Kennett (2002), Determination of the influence zone for surface wave paths, *Geophys. J. Int.*, *149*(2), 440–453.

Zhang, S., and S. Karato (1995), Lattice preferred orientation of olivine aggregates deformed in simple shear, *Nature*, *375*, 774–777.